



Single-crystalline porous NiO nanosheets prepared from β -Ni(OH)₂ nanosheets: Magnetic property and photocatalytic activity



Qiang Dong^{a,b,*}, Shu Yin^a, Chongshen Guo^a, Xiaoyong Wu^a, Nobuhiro Kumada^b,
Takahiro Takei^b, Akira Miura^b, Yoshinori Yonesaki^b, Tsugio Sato^a

^a Institute of Multidisciplinary Research for Advanced Materials, Tohoku University, 2-1-1 Katahira, Aoba-ku, Sendai 980-8577, Japan

^b Department of Research Interdisciplinary Graduate School of Medicine and Engineering, University of Yamanashi, Miyamae cho-7, Kofu 400-8511, Japan

ARTICLE INFO

Article history:

Received 12 June 2013

Received in revised form 3 October 2013

Accepted 7 October 2013

Available online 15 October 2013

Keywords:

Nickel oxide (NiO)

Porous nanosheets

Magnetic property

Photocatalytic activity

ABSTRACT

Nickel hydroxide (β -Ni(OH)₂) nanosheets with a diameter of 400 nm and a thickness of 20 nm were successfully synthesized by a template and surfactant-free solvothermal route in a very simple system composed of LiOH-H₂O and Ni-naphthenate. Furthermore, porous nickel oxide (NiO) nanosheets were obtained by thermal decomposition of β -Ni(OH)₂ nanosheets in air at 350–550 °C for 2 h. HRTEM and SAED results revealed that the microporous NiO nanosheets obtained at 350 °C were single-crystalline, and nitrogen adsorption–desorption measurements of the BET surface area and pore size of porous NiO nanosheets were 156 m² g⁻¹ and 1.7 nm, respectively. Moreover, mesoporous NiO nanosheets and macro-porous NiO nanosheets could be selectively obtained by controlling thermal decomposition temperature. The formation mechanism of porous NiO nanosheets was discussed. The magnetic property and photocatalytic activity of the porous NiO nanosheets were also investigated. The porous NiO nanosheets showed enhanced photocatalytic activity for NO destruction.

© 2013 Elsevier B.V. All rights reserved.

1. Introduction

Nanomaterials materials have attracted enormous attention due to their novel physical and chemical properties and promising applications [1,2]. The morphology, size, and crystallinity of the nanomaterial greatly influence their optical, electronic, magnetic, and catalytic properties [3–5]. Transitional metal oxides, such as cobalt [6–9], iron [10–14], and nickel [15,16], have attracted increasing interest owing to their potential in a variety of fields. Among them, nickel oxide (NiO), as a p-type wide band gap semiconductor [17], exhibits excellent performance for lithium ion batteries [18,19], fuel cells [20], supercapacitors [21], catalysts [22,23] and gas sensors [24–28]. The valuable functions greatly depend on the morphology and size of NiO nanostructures. To date, many efforts have been attempted to prepare NiO nanostructures, such as nano-ring [29], nano-ribbons [30], nano-wires [31], nano-tubes [32], nano-spheres [33]. In recent years, porous NiO nanosheets have been research hotspots due to the advantage of high specific surface area to enhance chemical/electrochemical activities. Huang et al. [34] prepared porous

NiO nanosheets/graphene hierarchical structure with a remarkable lithium-storage performance. Zhu et al. [35] synthesized porous NiO showing a high catalytic activity for CO oxidation. Alammar et al. [36] obtained mesoporous NiO nanosheets exhibiting excellent specific capacitance. Li et al. [37] reported the synthesis of porous NiO nanosheets used for formaldehyde sensing. However, some of the above-mentioned methods need high temperature, and the others need templates, which complicate the synthetic processes. Therefore, exploring new synthesis methods for porous NiO nanosheets will be useful to find new applications or to improve existing performance. On the other hand, considerable attention has been given to the environmental problem involving NO in air. Photocatalysis is a promising technology for the treatment of contaminants, especially for the decomposition of NO. Many investigations have been reported on utilizing metal oxide nanomaterials as photocatalysts for the decomposition of NO [38]. To the best of our knowledge, there is little research about the photocatalytic property of porous NiO nanosheets with high specific surface area, though other properties of porous NiO nanosheets have been widely investigated.

In the present work, we demonstrate an efficient and facile approach for the synthesis of β -Ni(OH)₂ nanosheets, which can be thermally decomposed to single-crystalline porous NiO nanosheets for the NO destruction. It is interesting to find the pore size of NiO nanosheets can be controlled by adjusting thermal decomposition temperature.

* Corresponding author at: Institute of Multidisciplinary Research for Advanced Materials, Tohoku University, 2-1-1 Katahira, Aoba-ku Sendai 980-8577, Japan.
Tel.: +81 22 217 5599; fax: +81 22 217 5598.

E-mail address: dong@tagen.tohoku.ac.jp (Q. Dong).

2. Experimental

2.1. Synthesis of β -Ni(OH)₂ nanosheets and porous NiO nanosheets

β -Ni(OH)₂ nanosheets: 15 ml of 6% nickel naphthenate ($[(R(CH_2)_nCOO^-)_2Ni^{2+}$, where R is a cyclopentyl or cyclohexyl group], DIC Co. Ltd.) xylene solution was added to 15 ml of LiOH solution (15 mol dm⁻³), where distilled water was used as a solvent at room temperature. Then, the green mixed solution was put in a 50 ml Teflon®-lined autoclave. The autoclave was sealed and maintained at 120 °C for 12 h, and then cooled to room temperature naturally. After centrifugation, the products were obtained and washed with distilled water and absolute ethanol two times and finally dried in air at 60 °C for 6 h.

Porous NiO nanosheets: as-prepared β -Ni(OH)₂ nanosheets were thermally decomposed at 350–550 °C for 2 h. Here, commercial NiO (Wako Pure Chemical Industries, Ltd) is used as a reference material.

2.2. Characterization

X-ray powder Diffraction (XRD) was performed on a Rigaku X-ray diffractometer (RINT2000V Japan) with graphite-monochromatized CuK α radiation ($\lambda = 1.54056 \text{ \AA}$) using 30 mA and 40 kV. The diffraction pattern over the range of 10–70° in 2θ was recorded with a scanning speed of 3°/min. Scanning electron microscopy (SEM) images were taken with JEOL JEM-6500F field emission scanning electron microscope. Transmission electron microscopy (TEM) images were taken with a JEOL JEM-2000FXII transmission electron microscope using an accelerating voltage of 200 kV. Thermo gravimetric analysis (TGA) was carried out in a Rigaku Thermal Plus TG 8120 thermal analysis system with a heating rate of 10 °C min⁻¹ from room temperature to 800 °C. The specific surface area and pore size distribution were measured using BET analysis (NOVA 4200e). UV-vis spectra were formed at room temperature on an UV-vis spectrophotometer (JASCO, V-670). Magnetic properties of porous NiO nanosheets were measured by utilizing a superconducting quantum interference device (SQUID) magnetometer in the magnetic property measurement system (MPMS) of Quantum Design (USA).

2.3. Photocatalytic degradation measurement

The photocatalytic activity of porous NiO nanosheets was investigated by evaluating the decomposition of NO (deNO_x) in a flow type reactor under irradiation of a 450 W high pressure mercury lamp at room temperature. The photocatalyst was spread in the hollow (20 mm × 16 mm × 0.5 mm) of a glass plate and then was

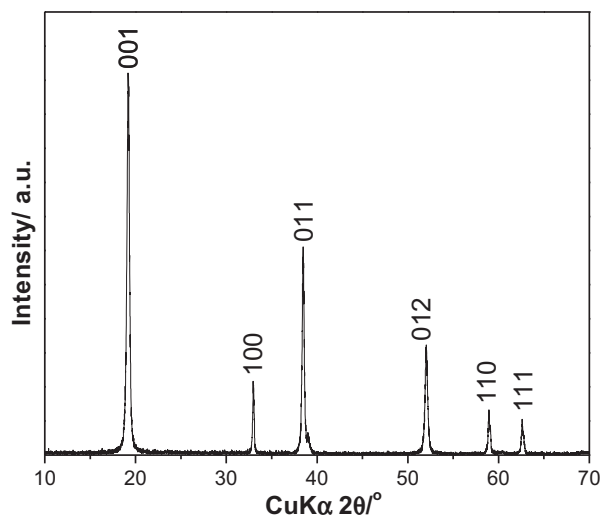


Fig. 1. XRD pattern of the obtained product prepared at 120 °C for 6 h.

placed at the bottom center of the reactor (373 cm³ of internal volume) in which a 1:1 mixed gas of air and nitrogen balanced 1 ppm of NO was flowed at the rate of 200 cm³ min⁻¹. The sample powder was kept in the dark for 30 min to reach the adsorption and desorption equilibrium of NO gas. After that, the mercury light was turned on to irradiate the sample, where the light wavelengths were controlled by several filters: Pyrex glass for >290 nm, Kenko L41 Super Pro (W) filter >400 nm and Fuji triacetyl cellulose filter >510 nm. The measuring time for each sample under each wavelength was 10 min [39]. The concentration of NO was checked by a NO_x analyzer (Yanaco, ECL-88A).

3. Results and discussion

Fig. 1 shows the XRD pattern of the obtained nickel hydroxide product. All the diffraction peaks could be indexed to a pure single phase of β -Ni(OH)₂ with the hexagonal structure according to the JCPDS 14-0117. The diffraction peak of (0 0 1) was the strongest in all the diffraction peaks shown in the XRD pattern, indicating the existence of an unusual nanostructure and preferential crystal growth.

The size and morphology of the as-prepared product are shown in Fig. 2. A great many of hexagonal β -Ni(OH)₂ nanosheets with good uniformity were observed (Fig. 2(a)). It was obvious that almost each of the β -Ni(OH)₂ nanosheet had clear corners and edges. The β -Ni(OH)₂ nanosheets with thickness of ~20 nm and edge size of ~200 nm were exhibited. The histogram shows the synthesized nanosheets had an average width of about 400 nm with

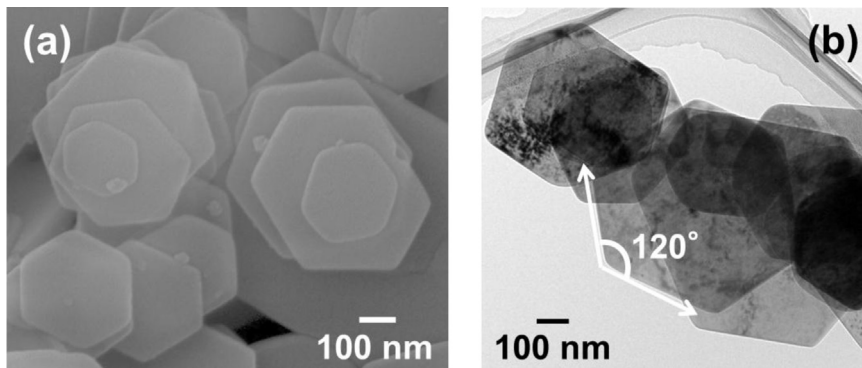


Fig. 2. SEM and TEM images of the obtained β -Ni(OH)₂ prepared at 120 °C for 6 h.

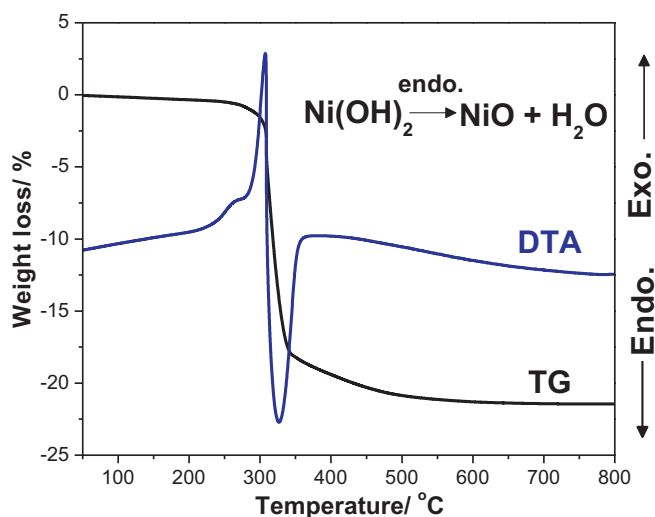


Fig. 3. The thermogravimetry–differential thermal analysis (TG–DTA) curves of the obtained β - $\text{Ni}(\text{OH})_2$ nanosheets.

little deviation (Fig. S1). The β - $\text{Ni}(\text{OH})_2$ nanosheets showed hexagonal and quasi-hexagonal with angles of adjacent edges of 120° (Fig. 2(b)).

Thermal decomposition temperature of the β - $\text{Ni}(\text{OH})_2$ nanosheets was examined by TG–DTA (Fig. 3) [40]. It was found that β - $\text{Ni}(\text{OH})_2$ started to decompose (accompanied with weight loss) at about 286°C . The major weight loss could be observed between ~ 308 and $\sim 345^\circ\text{C}$. Exothermic peak at 310°C could be attributed to the oxidative decomposition of organic phase (Ni-naphthenate) adsorbed on the surface of nanosheets. An endothermic peak with a maximum was located at 325°C . The total weight loss was $\sim 21\%$, and this value was very closely to the theoretical value (19.4%) [40]. It is indicated β - $\text{Ni}(\text{OH})_2$ converted into NiO during the thermal decomposition.

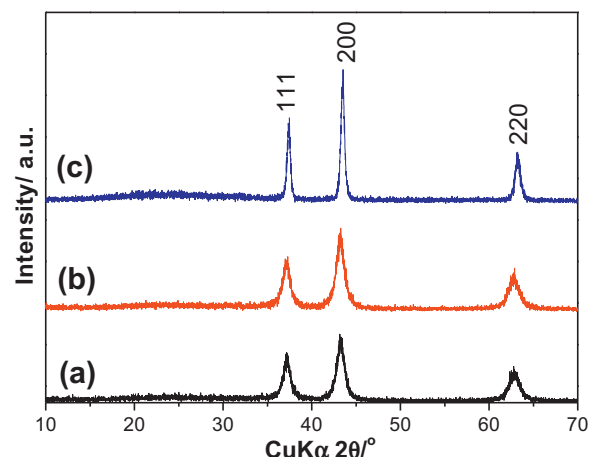


Fig. 4. XRD patterns of the products obtained from β - $\text{Ni}(\text{OH})_2$ nanosheets at different thermal decomposition temperatures for 2 h, respectively. (a) 350°C , (b) 450°C , and (c) 550°C .

On the basis of TG–DTA results, it is certain that β - $\text{Ni}(\text{OH})_2$ can decompose into NiO completely as temperature above 350°C . XRD patterns of NiO prepared by thermal decomposition of as-prepared β - $\text{Ni}(\text{OH})_2$ nanosheets at 350 – 550°C for 2 h are shown in Fig. 4. Only NiO peaks were detected for all the samples in Fig. 4, which could be indexed to the face-centered cubic (fcc) NiO phase (JCPDS 78-0643). The crystallinity of as-prepared NiO was improved with the decomposition temperature, indicating the increment of the crystal size of NiO. From the Scherrer equation, the average crystal size NiO increased from 6.4 to 23.1 nm (Fig. 4(a)–(c)).

The morphology of as-obtained NiO was investigated by SEM and TEM. Fig. 5(a) shows the NiO nanosheets prepared at 350°C (designated as NiO-350) exhibiting rough surface with a diameter of ~ 400 nm. As the thermal decomposition temperature increased to 450°C , the morphology of these small-crystallized 2D NiO nanosheets (designated as NiO-450) was like a lotus-root, including

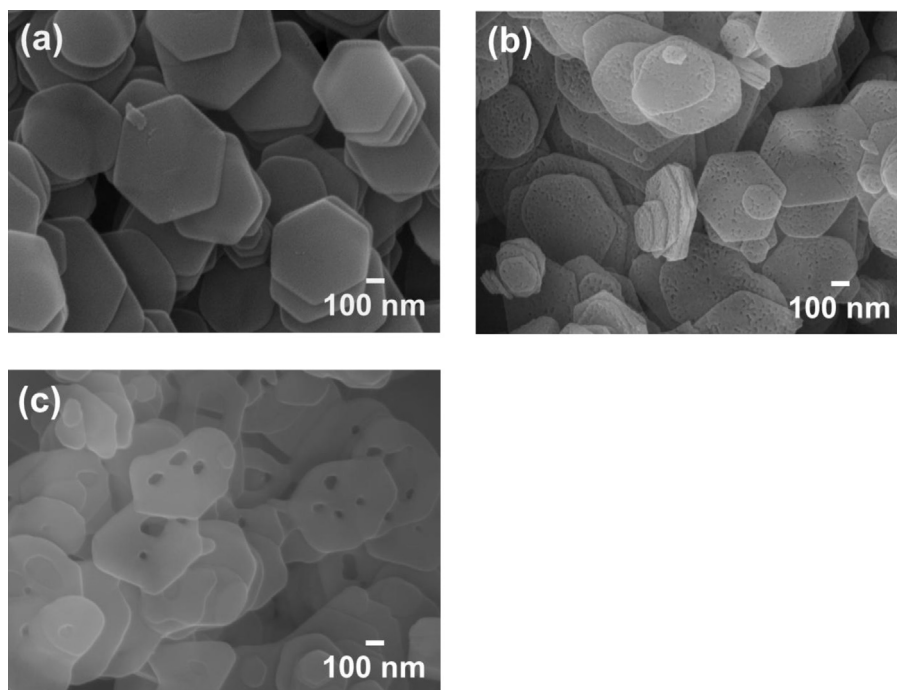


Fig. 5. SEM images of the NiO obtained from β - $\text{Ni}(\text{OH})_2$ nanosheets at different thermal decomposition temperatures for 2 h, respectively. (a) 350°C , (b) 450°C , and (c) 550°C .

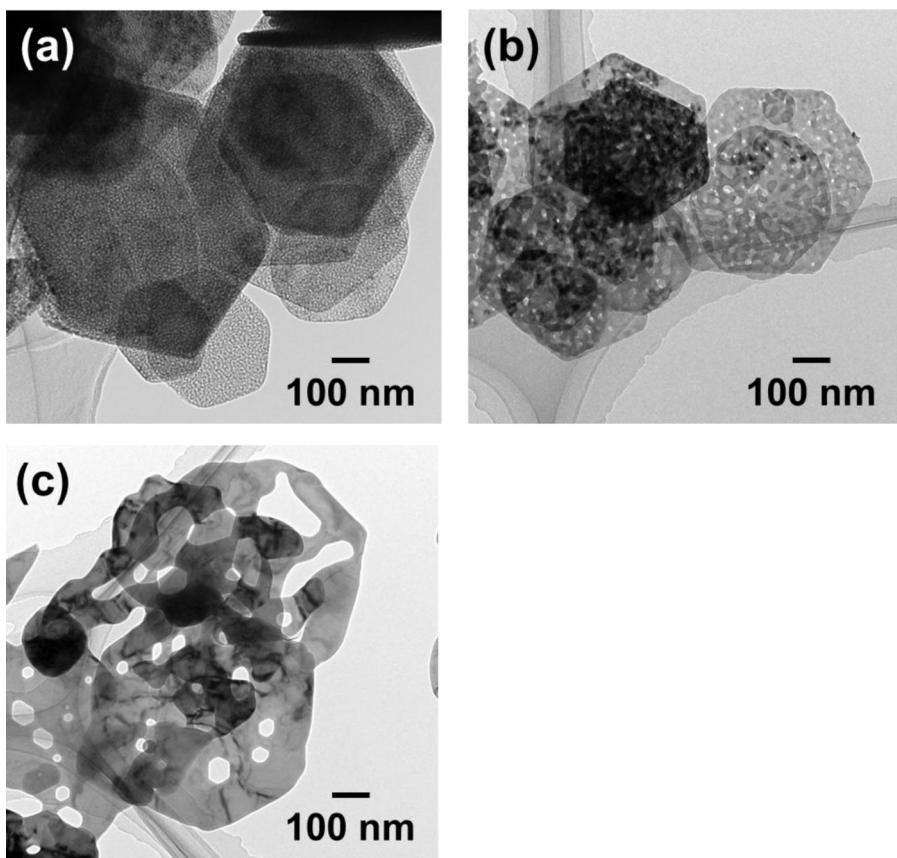


Fig. 6. TEM images of the different NiO. (a) NiO-350, (b) NiO-450, and (c) NiO-550.

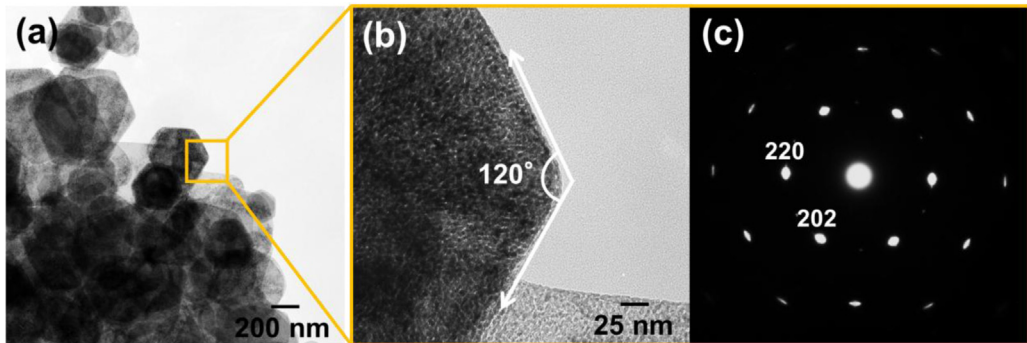


Fig. 7. (a) TEM image of the NiO-350 nanosheets; (b) HRTEM image of the selected NiO-350 nanosheet; (c) SAED pattern of the selected NiO-350 nanosheet.

mesopores with a mean diameter of ~10 nm (Fig. 5(b)). The size of macropores of NiO nanosheets at 550 °C (designated as NiO-550) increased to 50 nm (Fig. 5(c)). Hexagonal NiO nanorings could be obtained as the calcination temperature increased to 650 °C (Fig. S2). For the comparison, the morphology of commercial NiO was also investigated by TEM. As a result, commercial NiO exhibited irregular particles with a mean diameter of ~600 nm shown in Fig. S3.

From the Fig. 6(a), it is clear that nanosheets with micropores have been obtained by calcination of the as-prepared β -Ni(OH)₂ nanosheets in air at 350 °C for 2 h. The size of the pores increased with the thermal decomposition temperature, and the results of TEM agreed with those of SEM images.

It is expedient to classify pores according to their sizes. Pores with widths exceeding about 50 nm are called macropores; pores of widths between 2 nm and 50 nm are called mesopores; pores with widths not exceeding about 2 nm are called micropores [41].

For the microporous NiO-350 nanosheets, under careful observation, the NiO nanosheets were found to be composed of many pores with a mean diameter of ~2 nm (Fig. 7(a) and (b)). The porous NiO nanosheets also consisted of hexagonal and quasi-hexagonal structures of adjacent edges of 120°. The inset of Fig. 7(c) is an SAED pattern taken from an individual NiO nanosheet; The SAED pattern indicated that porous NiO nanosheet consisted of a single-crystalline in structure. All spots can be indexed to the face-centered cubic (fcc) NiO, being consistent in the XRD result.

Generally, specific surface area and pore diameter play a part in determining the electrochemistry, gas sensor and catalysis properties of the active materials [38,42]. The surface area and pore size distribution of porous NiO nanosheets were investigated using nitrogen adsorption and desorption isotherms. NiO-350 exhibited a high BET specific surface area of 156 m² g⁻¹ with a pore volume of 0.9 cm³ g⁻¹. The sharp pore size distribution with a single modal centered at 1.7 nm (Fig. 8 inset, Fig. S4) were shown through the

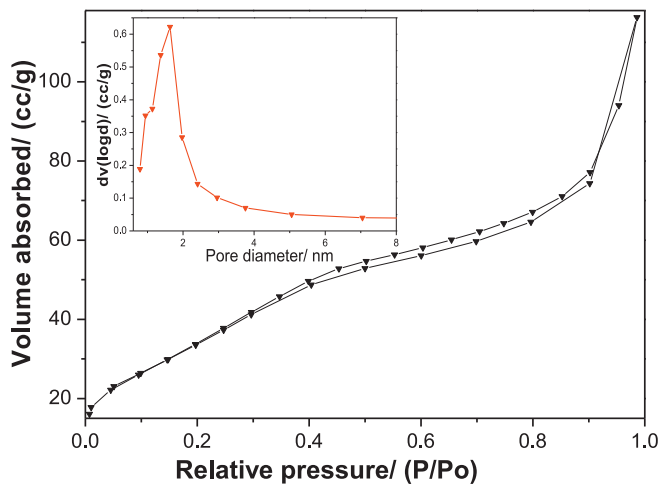


Fig. 8. Nitrogen adsorption and desorption isotherms of the NiO-350, inset shows the pore size distribution curve.

desorption isotherm, and the result agreed with that of TEM image. The BET specific surface area decreased to 52 and $26 \text{ m}^2 \text{ g}^{-1}$ as the thermal decomposition temperature increased to 450°C (NiO-450) and 550°C (NiO-550), meanwhile, the pore volume decreased to 0.4 and $0.1 \text{ cm}^3 \text{ g}^{-1}$, respectively. All the as-prepared porous NiO nanosheets showed the relatively high surface area compared to commercial NiO particles ($18 \text{ m}^2 \text{ g}^{-1}$).

Herein, a possible mechanism of the formation of hexagonal $\beta\text{-Ni(OH)}_2$ nanosheets and porous NiO nanosheets is suggested, which is similar to the that of $\beta\text{-Co(OH)}_2$ nanosheets and porous Co_3O_4 [43]. A crystal-growth process is considered in the formation of the hexagonal $\beta\text{-Ni(OH)}_2$ nanosheets. Firstly, $\beta\text{-Ni(OH)}_2$ crystal nuclei are formed, then these nuclei grow up into hexagonal nanosheets during crystal growth. Nickel naphthenate might play a crucial role in this process. Nickel naphthenate was used as a reagent to provide both a nickel element and a surface modifier, such as cyclopentyl complexing reagent to influence the growth of the particles. Our previous experimental results indicated that cobalt naphthenate might provide strong kinetic control over the growth rates of various faces of $\beta\text{-Co(OH)}_2$ by being selectively adsorbed on the crystal planes, resulting in the formation of hexagonal $\beta\text{-Co(OH)}_2$ nanosheets [44]. Other conditions remain the same, the $\text{Ni}(\text{NO}_3)_2\cdot6\text{H}_2\text{O}$ was used as nickel source instead of nickel naphthenate, only irregular NiO nanoparticles with the size of $\sim 300 \text{ nm}$ could be obtained (Fig. S5). The result indicated that nickel naphthenate is not only a reagent to provide a nickel element, but also a surface modifier. Ni-OH layers and counter anions between the Ni-OH layers were included in the crystal structure of the hexagonal $\beta\text{-Ni(OH)}_2$ nanosheets. Under pyrolysis and dehydration, the Ni-OH layers were converted into nickel oxide with the increasing of thermal decomposition temperature. As a result, the spaces of the OH layers and counter anions led to the formation of nanopores. The calcination temperature is also especially important in the formation of NiO nanosheets and nanorings. With the calcination temperature increased, the $\beta\text{-Ni(OH)}_2$ nanosheets gradually dehydrated and shrank from the pores, the area with perfect crystallization underwent a low decomposition rate which well remained hexagonal shape but observed larger pores and formed defects or poor crystallization areas and the hexagonal shape nanosheets were converted into porous nanosheets and nanorings. “Second grains” are the porous NiO nanosheets derived from the thermal decomposition of the hexagonal $\beta\text{-Ni(OH)}_2$ nanosheets. “Primary pores” is denoted for the aggregated micropores in the hexagonal NiO nanosheets. With increasing of thermal decomposition temperature, the reaction of pyrolysis and dehydration took

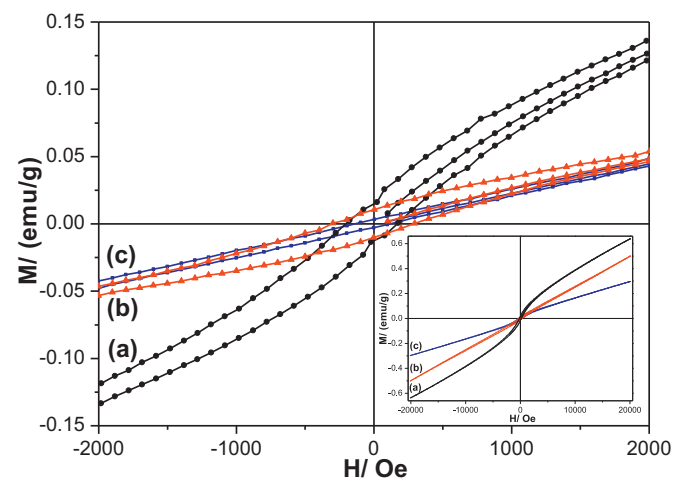


Fig. 9. Magnetite hysteresis (MH) curves measured at 5 K for porous NiO nanosheets. (a) NiO-350, (b) NiO-450, and (c) NiO-550.

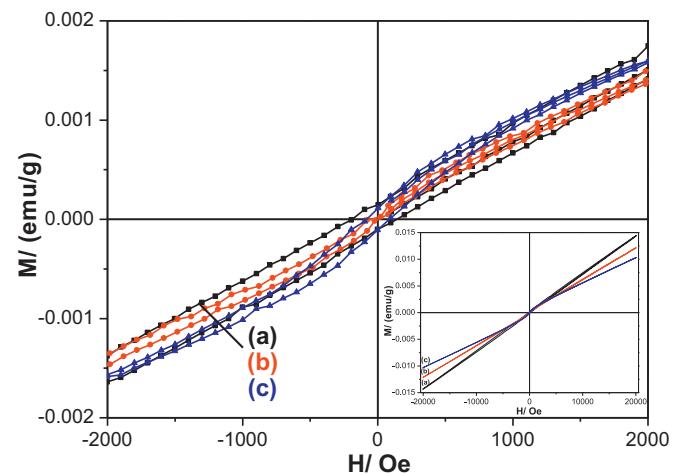


Fig. 10. Magnetite hysteresis (MH) curves measured at 300 K for porous NiO nanosheets. (a) NiO-350, (b) NiO-450, and (c) NiO-550.

on the boundary of “primary pores”, the “primary pores” in the aggregates transfer to form larger pores. As a result, with increasing the thermal decomposition temperature results in gathering of the small pores to form large pores. Our synthetic strategy may be employed to prepare porous nanosheets with different pore sizes of other metal oxides by the thermal decomposition of corresponding metal hydroxide nanosheets under appropriate conditions.

From Fig. 9, small hysteresis loops at a low field could be observed for all the porous NiO nanosheets, indicating the existence of a weak ferromagnetic component. This result suggests that the obtained porous NiO nanosheets are ferromagnetic and different from the bulk NiO, which is antiferromagnetic [45]. The magnetic hysteresis loops showed that the saturated magnetic (M_s) moment of NiO-350, NiO-450 and NiO-550 at 5 K were 0.017, 0.013, and 0.009 emu g^{-1} , respectively. Magnetization value invariably decreased with increasing crystal size, i.e., increasing thermal decomposition temperature [46,47]. Duan et al. reported magnetization behavior increased with surface spins, which decreased with an increase in the particle size [48]. In this work, the crystal size of NiO increases with a decrease in the surface area, which may be leading to the decrement of surface spins. As a result, magnetization value decreased with surface area. The magnetic properties of porous NiO nanosheets at 300 K were also investigated (Fig. 10). All the

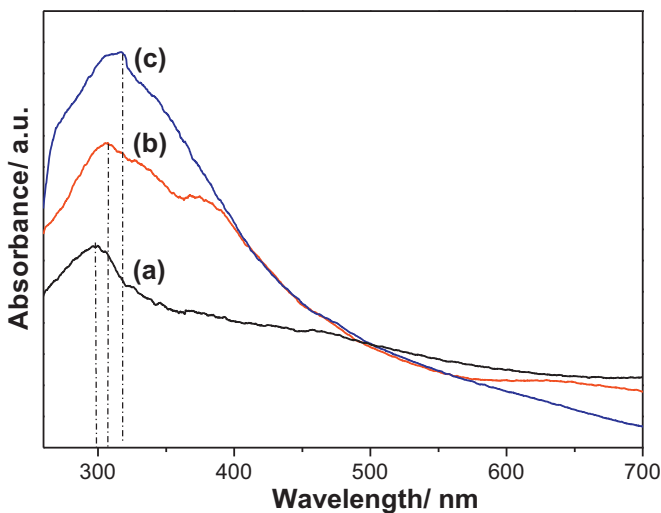


Fig. 11. UV-vis adsorption spectra of porous NiO nanosheets. (a) NiO-350, (b) NiO-450, and (c) NiO-550.

magnetic hysteresis loops showed antiferromagnetic properties. Moreover, the temperature dependence of magnetization of NiO-350 with a field of $H = 20$ kOe under both field cooled (FC) and zero field cooled (ZFC) conditions was also tested (Fig. S3). Bifurcation of the FC and ZFC curves below a particular temperature ($T_b \sim 280$ K). The ZFC curve shows a weak broad maximum centered at $T_p \sim 85$ K. Above the bifurcation temperature (T_b) magnetization FC and ZFC curves exhibit superparamagnetic characteristics [47,49].

The UV-vis absorption spectra of the as-prepared NiO-350, NiO-450, and NiO-550 are illustrated in Fig. 11. It could be seen that the morphological changes of the NiO were accompanied by remarkable changes in the UV-vis spectra because of the significant difference in crystal size and pore size [50]. It could be accepted that with a small pore size allows multiple reflections of UV light within the interior cavity [51], resulting a decrease on absorbance. As the reflections of UV light decreased with an increase of pore size, on the contrary, absorbance increased. It is well known that the bandgap energy of semiconductor nanoparticles increases with the decrease in particle size. In our case, a shift of the peak (from ca. 317 to 298 nm) was observed when the average Scherrer crystal size of the porous NiO nanosheets decreased from 23.1 to 6.4 nm (Fig. 4).

To investigate the relationship between the morphology and photocatalytic property, we implemented oxidative destruction of NO of the porous NiO nanosheets prepared at different thermal decomposition temperatures. Fig. 12 shows the deNO_x ability of porous NiO nanosheets synthesized at different temperatures, together with that of commercial particles, where the different wavelength lights (>510 nm, >400 nm and >290 nm) were irradiated to the samples. Although the deNO_x ability of porous NiO nanosheets inferior to that of other metal oxides such as TiO₂ [52], the NiO-350 showed significantly higher activities than those of NiO-450, NiO-550 and commercial NiO under the same wavelength light irradiation. The results indicated that photocatalytic activity decreased with the increment of specific surface area of the NiO nanosheets. It could be clearly seen that the deNO_x ability of NiO-350, NiO-450, NiO-550 and commercial NiO were about 42, 25, 22 and 19% under the irradiation of light wavelength >290 nm, respectively. Moreover, under the irradiation of >290 nm light, the deNO_x of NiO-350 is higher than those of TiO₂ (40%) [53] and H₄Nb₆O₁₇/n-C₃H₇NH₂ (18%) catalysts [54]. The stability of deNO_x ability of sample NiO-350 with the induction of 290 nm light was shown in Fig. S6. It is apparent that the UV light induced deNO_x ability of

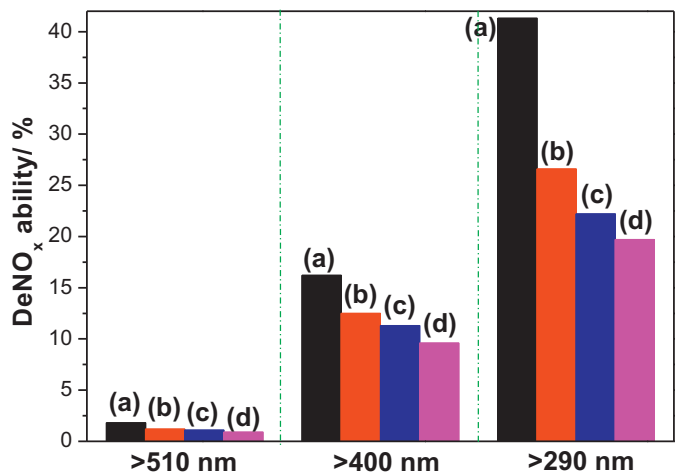
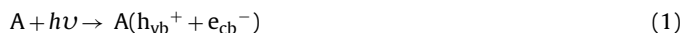


Fig. 12. deNO_x ability of the porous NiO nanosheets. (a) NiO-350, (b) NiO-450, (c) NiO-550, and (d) Commercial NiO.

NiO-350 presented no big difference after 3 runs, implying that the NiO-350 had a good stability for NO_x destruction when irradiated by UV light. Such dramatic activity enhancement should be due to the change of specific surface area. The specific surface area of NiO-350, NiO-450, NiO-550 and commercial NiO were 156, 52, 26 and 18 m² g⁻¹, respectively. With a larger surface area, the number of active surface sites increases to enhance the surface charge carrier transfer rate in photocatalysis [51]. On the other hand, considering the size of porous nanosheets is quite close to each other, the change of specific surface area is caused by different pore sizes, it is more clearly that photocatalytic activity decreased with the increment of pore size. It has been accepted generally that photocatalyst particles (denoted as A) absorb light of energy greater than the band gap to generate electron/hole pairs (Eq. (1)). The electrons are photoinduced to conduction band (e_{cb}⁻), and the holes in valence band (h_{vb}⁺) [55].



For the NiO in this work, the decomposition path of NO is similar to that of titania particles synthesized by Yin [56]. Electron/hole pairs are formed by the photoexcitation of NiO (Eq. (2)). In the presence of oxygen, these photoinduced electrons are immediately trapped by the molecular oxygen to form •O₂⁻ (Eq. (3)) and •OOH radicals (Eq. (4)) [57]. On the other hand, the holes are trapped by water in the air to produce hydroxyl radicals (Eq. (5)) [58].



During the decomposition of NO, oxidation occurs through active oxygen species, such as •OH and •O₂⁻ displayed in Eqs. (6)–(8) [59,60]. NO could react with these reactive radicals, molecular oxygen, and a very small amount of water in the air to produce HNO₂ or HNO₃. In the NO_x atmosphere, the NO_x molecule may have trapped the superoxide radical •O₂⁻ to form NO₃⁻ (Eq. (8)).



Since there were few reports on the photocatalytic activity of porous NiO nanosheets, our findings suggested that porous NiO nanosheets could be used in environmental applications, such as organic pollutant purification, and air purification.

4. Conclusions

In summary, β -Ni(OH)₂ nanosheets were successfully synthesized by choosing nickel naphthenate as a reagent to produce both the nickel element and a surface modifier complexing reagent under solvothermal condition at such low temperature as 120 °C. This is a simple and low-cost method, being applicable for the large-scale production of powders of β -Ni(OH)₂ nanosheets. Notably, single-crystalline porous NiO nanosheets have been successfully prepared by the thermal decomposition of β -Ni(OH)₂ nanosheets precursor at 350 °C. Microporous, mesoporous and macroporous NiO nanosheets could be selectively obtained by controlling the thermal decomposition temperature. The thermal decomposition temperature is an especially important point in determining pore size and finally resulted in changes of the morphology and property of NiO nanosheets. The as obtained porous NiO nanosheets showed high photocatalytic deNO_x property, displaying great potential in the application of environmental pollutant cleanup. The synthetic strategy may be employed to prepare porous nanosheets with different pore sizes of other metal oxides.

Acknowledgments

This work was partly supported by Grant-in-Aid for Young Scientists B (25870054) from the Japan Society for the Promotion of Science (JSPS), Rare Metal Substitute Materials Development Project of New Energy and Industrial Technology Development Organization (NEDO), Japan and the Management Expenses Grants for National Universities Corporations and the Grants-in-Aid for Scientific Research Program for Challenging Exploratory Research from the Ministry of Education, Culture, Sports and Science for Technology of Japan (MEXT).

Appendix A. Supplementary data

Supplementary data associated with this article can be found, in the online version, at <http://dx.doi.org/10.1016/j.apcatb.2013.10.007>.

References

- [1] T. Rueckes, K. Kim, E. Joselevich, G.Y. Tseng, C.L. Cheung, C.M. Lieber, *Science* 289 (2000) 94–97.
- [2] Y. Cui, C.M. Lieber, *Science* 291 (2001) 851–853.
- [3] V.I. Klimov, *Annu. Rev. Phys. Chem.* 58 (2007) 635–673.
- [4] L. Li, J. Hu, W. Yang, A.P. Alivisatos, *Nano Lett.* 1 (2001) 349–351.
- [5] N.I. Kovtyukhova, T.E. Mallouk, *Chem. Eur. J.* 8 (2002) 4354–4363.
- [6] J.T. Sampanthar, H.C. Zeng, *J. Am. Chem. Soc.* 124 (2002) 6668–6675.
- [7] Y. Hou, H. Kondoh, M. Shimojo, T. Kogure, T. Ohta, *J. Phys. Chem. B* 109 (41) (2005) 19094–19098.
- [8] Q. Dong, N. Kumada, Y. Yonesaki, T. Takei, N. Kinomura, *J. Ceram. Soc. Jpn.* 119 (2011) 538–540.
- [9] Q. Dong, S. Yin, C.S. Guo, H.H. Li, Y.F. Huang, N. Kumada, T. Takei, Y. Yonesaki, T. Sato, *Int. J. Nanotechnol.* 10 (2013) 71–79.
- [10] X. Wang, X. Chen, L. Gao, H. Zheng, M. Ji, C. Tang, T. Shen, Z. Zhang, *J. Mater. Chem.* 14 (2004) 905–915.
- [11] Q. Dong, D. Wang, J.X. Yao, N. Kumada, N. Kinomura, T. Takei, Y. Yonesaki, Q. Cai, *J. Ceram. Soc. Jpn.* 117 (2009) 245–248.
- [12] Q. Dong, N. Kumada, Y. Yonesaki, T. Takei, N. Kinomura, *J. Ceram. Soc. Jpn.* 117 (2009) 881–886.
- [13] Q. Dong, N. Kumada, Y. Yonesaki, T. Takei, N. Kinomura, *J. Ceram. Soc. Jpn.* 118 (2010) 272–277.
- [14] Q. Dong, N. Kumada, Y. Yonesaki, T. Takei, N. Kinomura, D. Wang, *J. Mater. Sci.* 45 (2010) 5685–5691.
- [15] D. Yang, R. Wang, M. He, J. Zhang, Z.F. Liu, *J. Phys. Chem. B* 109 (2005) 7654–7658.
- [16] Y. Nuli, S. Zhao, Q. Qin, *J. Power Sources* 114 (2003) 113–120.
- [17] B. Sasi, K.G. Gopchandran, *Nanotechnology* 18 (2007) 115613–115621.
- [18] B. Varghese, M. Reddy, Z. Yanwu, C. Lit, T. Hoong, G. Rao, B. Chowdari, A. Wee, C. Lim, C. Sow, *Chem. Mater.* 20 (2008) 3360–3367.
- [19] L. Liu, Y. Li, S. Yuan, M. Ge, M. Ren, C. Sun, Z. Zhou, *J. Phys. Chem. C* 114 (2010) 251–255.
- [20] B. Park, E. Cairns, *J. Electrochem. Commun.* 13 (2011) 75–77.
- [21] S.I. Kim, J.S. Lee, H.J. Ahn, H.K. Song, J.H. Jang, *ACS Appl. Mater. Interfaces* 5 (2013) 1596–1603.
- [22] B. Zhao, X. Ke, J. Bao, C. Wang, L. Dong, Y. Chen, H. Chen, *J. Phys. Chem. C* 113 (2009) 14440–14447.
- [23] N. Berguerand, F. Lind, M. Israelsson, M. Seemann, S. Biollaz, H. Thunman, *Ind. Eng. Chem. Res.* 51 (2012) 16610–16616.
- [24] J.A. Dirksen, K. Duval, T.A. Ring, *Sens. Actuators B* 80 (2001) 106–115.
- [25] I. Hotovy, V. Rehacek, P. Siciliano, S. Capone, L. Spiess, *Thin Solid Films* 418 (2002) 9–15.
- [26] I. Hotovy, J. Huran, P. Siciliano, S. Capone, L. Spiess, V. Rehacek, *Sens. Actuators B* 78 (2001) 126–132.
- [27] N.D. Hoa, S.A. El-Safty, *Chem.-Eur. J.* 17 (2011) 12896–12901.
- [28] G.X. Zhu, C.Y. Xi, H. Xu, D. Zheng, Y.J. Liu, X. Xua, X.P. Shen, *RSC Adv.* 2 (2012) 4236–4241.
- [29] J. Liang, Y.D. Li, *Chem. Lett.* 32 (2003) 1126–1127.
- [30] X.M. Ni, Q.B. Zhao, F. Zhou, H.G. Zheng, J. Cheng, B.B. Li, *J. Cryst. Growth* 289 (2006) 29.
- [31] Z.Y. Wu, C.M. Liu, L. Guo, R. Hu, M.I. Abbas, T.D. Hu, H.B. Xu, *J. Phys. Chem. B* 109 (2005) 2512–2515.
- [32] G. Malandrino, L.M.S. Perdicaro, I.L. Fragala, R.L. Nigro, M. Losurdo, G. Bruno, *J. Phys. Chem. C* 111 (2007) 3211.
- [33] X.M. Sun, J.F. Liu, Y.D. Li, *Chem. Eur. J.* 12 (2006) 2039–2047.
- [34] Y. Huang, X.L. Huang, J.S. Lian, D. Xu, L.M. Wang, X.B. Zhang, *J. Mater. Chem.* 22 (2012) 2844–2847.
- [35] J.X. Zhu, Z. Gui, Y.Y. Ding, Z.Z. Wang, Y. Hu, M.Q. Zou, *J. Phys. Chem. C* 111 (2007) 5622–5627.
- [36] T. Alammar, O. Shekhah, J. Wohlgemuth, A.V. Mudring, *J. Mater. Chem.* 22 (2012) 18252–18260.
- [37] G.H. Li, X.W. Wang, H.Y. Ding, T. Zhang, *RSC Adv.* 2 (2012) 13018–13023.
- [38] X.B. Chen, S.S. Mao, *Chem. Rev.* 107 (2007) 2891–2959.
- [39] S. Yin, M. Komatsu, Q.W. Zhang, F. Saito, T. Sato, *J. Mater. Sci.* 42 (2007) 2399–2404.
- [40] Z.H. Liang, Y.J. Zhu, X.L. Hu, *J. Phys. Chem. B* 108 (2004) 3488–3491.
- [41] K.S.W. Sing, D.H. Everett, R.A.W. Haul, L. Moscou, R.A. Pierotti, J. Rouquerol, T. Siemieniewaka, *Pure Appl. Chem.* 57 (1985) 603–619.
- [42] J. Chang, J. Sun, C.H. Xu, H. Xu, L. Gao, *Nanoscale* 4 (2012) 6786–6791.
- [43] X.H. Liu, R. Yi, N. Zhang, R.R. Shi, X.G. Li, G.Z. Qiu, *Chem. Asian J.* 3 (2008) 732–738.
- [44] Q. Dong, N. Kumada, Y. Yonesaki, T. Takei, N. Kinomura, *Mater. Res. Bull.* 46 (2011) 1156–1162.
- [45] H. Pang, Q.Y. Lu, Y.C. Lia, F. Gao, *Chem. Commun.* 48 (2009) 7542–7544.
- [46] Y. Ichiyangagia, N. Wakabayashi, J. Yamazaki, S. Yamada, Y. Kimishima, E. Komatsu, H. Tajima, *Physica B* 329–333 (2003) 862–863.
- [47] S. Thota, J. Kumar, *J. Phys. Chem. Solids* 68 (2007) 1951–1964.
- [48] W.J. Duan, S.H. Lu, Z.L. Wu, Y.S. Wang, *J. Phys. Chem. C* 116 (2012) 26043–26051.
- [49] A.K. Mishra, S. Bandyopadhyay, D. Das, *Mater. Res. Bull.* 47 (2012) 2288–2293.
- [50] X.F. Song, L. Gao, *J. Phys. Chem. C* 112 (2008) 15299–15305.
- [51] H.X. Li, Z.F. Bian, J. Zhu, D.Q. Zhang, G.S. Li, Y.N. Huo, H. Li, Y.F. Lu, *J. Am. Chem. Soc.* 129 (2007) 8406–8407.
- [52] Y.L. Wei, Y.F. Huang, J.H. Wu, M. Wang, C.S. Guo, Q. Dong, S. Yin, T. Sato, J. Hazard. Mater. 248–249 (2013) 202–210.
- [53] X.Y. Wu, S. Yin, Q. Dong, C.S. Guo, T. Kimura, J.I. Matsushita, T. Sato, *J. Phys. Chem. C* 117 (2013) 8345–8352.
- [54] P.L. Zhang, S. Yin, R.X. Li, T. Sato, *J. Ceram. Soc. Jpn.* 115 (2007) 898–900.
- [55] S. Yin, D. Maeda, M. Ishitsuka, J.H. Wu, T. Sato, *Solid State Ionics* 151 (2002) 377–383.
- [56] S. Yin, B. Liu, P.L. Zhang, T. Morikawa, K.I. Yamanaka, T. Sato, *J. Phys. Chem. C* 112 (2008) 12425–12431.
- [57] S. Yin, T. Sato, *Ind. Eng. Chem. Res.* 39 (2000) 4526–4530.
- [58] M.R. Hoffmann, S.T. Martin, W. Choi, D.W. Bahnemann, *Chem. Rev.* 95 (1995) 69–96.
- [59] J.S. Dalton, P.A. Janes, N.G. Jones, J.A. Nicholson, K.R. Halam, G.C. Allen, *Environ. Pollut.* 120 (2002) 415–442.
- [60] M. Anpo, *Recent Developments on Visible Light Response Type Photocatalysts*, NTS, Tokyo, ISBN 4-86043-009-03, 2002, p. 9.